Computer Methods in Applied Mechanics and Engineering 425 (2024) 116911

Contents lists available at ScienceDirect

Computer Methods in Applied Mechanics and Engineering

journal homepage: www.elsevier.com/locate/cma

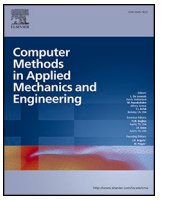

Dynamic optimisation for graded tissue scaffolds using machine learning techniques

Chi Wu [a], Boyang Wan [a], Yanan Xu [a], D S Abdullah Al Maruf [b,c], Kai Cheng [d], William T Lewin [e,f,i], Jianguang Fang [g], Hai Xin [b,c], Jeremy M Crook [e,f,h,i], Jonathan R Clark [b,c,d], Grant P Steven [a], Qing Li [a,*]

[a] School of Aerospace, Mechanical and Mechatronic Engineering, The University of Sydney, Sydney, NSW 2006, Australia
[b] Integrated Prosthetics and Reconstruction, Department of Head and Neck Surgery, Chris O'Brien Lifehouse, Camperdown, NSW 2050, Australia
[c] Central Clinical School, Faculty of Medicine and Health, The University of Sydney, Camperdown, NSW 2050, Australia
[d] Royal Prince Alfred Institute of Academic Surgery, Sydney Local Health District, Camperdown, NSW 2050, Australia
[e] Arto Hardy Family Biomedical Innovation Hub, Chris O`Brien Lifehouse, Camperdown, NSW 2050, Australia
[f] Sarcoma and Surgical Research Centre, Chris O'Brien Lifehouse, Camperdown, Australia
[g] School of Civil and Environmental Engineering, University of Technology Sydney, Sydney, NSW 2007, Australia
[h] Intelligent Polymer Research Institute, AIIM Facility, The University of Wollongong, Wollongong, Australia
[i] School of Medical Sciences, Faculty of Medicine and Health, The University of Sydney, Camperdown, Australia

ARTICLE INFO

Keywords:
Functionally-graded tissue scaffolds
Dynamic topology optimisation
Machine learning
Sheep mandible
Bone remodelling
Homogenisation

ABSTRACT

Tissue scaffolds have emerged as a promising solution for treatment of critical size bone defects, offering significant advantages over conventional strategies. One of the key functionalities of bone scaffolds is their ability to promote long-term bone ingrowth effectively. To enhance this functionality, we develop a novel dynamic optimisation framework to customise bone scaffolds for achieving maximum bone ingrowth outcomes over a certain period in this study. To improve the design efficiency, we extensively leverage machine learning (ML) techniques within our proposed dynamic optimisation framework. Specifically, two neural networks are integrated into a dynamic bone growth model, and another neural network is coupled with a genetic algorithm for dynamic optimisation process. To demonstrate the effectiveness and efficiency of the approach, we employ a sheep mandible reconstruction for treating a critical size bone defect as an illustraive example. To validate the finite element (FE) model established, we first conduct a mechanical test on the sheep mandible assembled with a tailored 3D printed scaffold made of Polyetherketone (PEK) material. Then, we compare three different optimisation schemes, namely uniform design, lateral gradient design, and vertical gradient design, with an empirical design under the same biomechanical conditions. A 18.5 % enhancement is found in the long-term bone ingrowth when the optimised scaffold is adopted in comparison with the empirical design, which is attributed to the fine-tuning of strut sizes within lattice scaffold structures for facilitating bone regeneration in the gradient regions. This study proposes a novel design framework by combining ML and time-dependent topology optimisation, which provides a new methodology for developing innovative tissue scaffolds with better clinical outcomes.

* Corresponding author.
E-mail address: qing.li@sydney.edu.au (Q. Li).

https://doi.org/10.1016/j.cma.2024.116911
Received 4 October 2023; Received in revised form 29 January 2024; Accepted 6 March 2024
Available online 23 March 2024

1. Introduction

Musculoskeletal disorders are among the most severe conditions that reduce patient's ability to work and maintain quality of life. The demand for reconstructive surgeries to address critical size bone defects has dramatically increased worldwide as a result of injuries, trauma, cancer and other diseases [1]. However, conventional treatments involving autografts or allografts face inherent problems, including risks of infection, rejection, disease transmission, donor site morbidity, and limited tissue supply [2]. To overcome these limitations, researchers have paid substantial attention on bone scaffolds as alternative substitutes for autografts/allografts [3].

Bone scaffolds are composed of porous structures that support cell attachment, migration, proliferation, and differentiation, thereby promoting the formation of bony tissue on the surfaces and spaces of pores [4]. Recent advancements in manufacturing techniques have greatly alleviated the limitations in fabricating highly sophisticated porous geometries of scaffold structure [5], leading to significant research efforts in innovative development of bone scaffolds with intricate constructs and desired functionalities [6].

From a design perspective, development of tissue scaffolds can be typically classified as mechanical property driven and bone ingrowth driven [7]. In mechanical property driven design, one of the primary interests is to attain desired effective moduli, strength and diffusivity/permeability of tissue scaffolds [8,9]. For instance, Uth et al. [10] developed synthetic scaffolds composed of poly, type I collagen and nano-hydroxyapatite, in which they optimised the diameters of scaffold struts to maximise compressive moduli. Another important aspect of the mechanical property driven design is tailoring scaffold porosity/tortuosity or permeability/diffusivity to facilitate proper mass transport for nutrient delivery and waste metabolism. For example, Poh et al. [11] employed a density-based topology optimisation to tailor the distribution of scaffold porosity subject to a stiffness constraint. Table 1 summarises additional studies on the mechanical property driven design of bone scaffolds for desired moduli, strength, and diffusivity/permeability.

Bone scaffolds are used to replace bony tissue with the primary objectives of ensuring sufficient stabilisation in surgical areas and promoting skeletal tissue regeneration [2]. *In-vivo* studies have shown that mechanical stimuli generated by external physical loads in localised regions play a vital role in tissue ingrowth [12]. Rooted on this premise, several studies have been conducted to design bone scaffolds for fostering the development of newly formed bony tissue within scaffolds [13–19], which fall under the category of bone growth driven design. Such bone growth driven design studies can be further classified into two groups in general: namely time-independent design and time-dependent design.

In a time-independent design, several key structural factors that significantly influence bone formation are commonly taken into account in the initial stage. For example, scaffolds have been customised to mimic elastic properties of host natural bone, thereby generating similar mechanical environment to promote bone growth when subjected to external physiological loading at the beginning of scaffolding [20]. Other studies have focused on reducing stress shielding or achieving an initial uniform stress/strain pattern to facilitate uniform bone growth within bulk scaffolds [21,22]. Furthermore, wall shear stress has also been considered a time-independent design criterion to promote bone growth [23].

Nevertheless, Perier-Metz et al. [24] pointed out that time-dependent design could be more meaningful in achieving a desirable long-term therapeutical outcome. They have demonstrated that initially optimised mechanical conditions may not ensure an optimal long-term bone regeneration, as the newly formed bone would gradually change the mechanical conditions within a scaffold in a dynamic manner. Building upon this concept, several studies have explored the "time-dependent" design to maximise long-term bone ingrowth outcomes [13–16,25–27]. Table 1 outlines the literature studies focusing on bone growth outcomes with both

Table 1
Design optimisation of tissue scaffolds: mechanical property driven and tissue growth driven studies.

Refs	Design type	Design variables	Design objectives
[10,28]	Mechanical properties	Strut size	Compressive modulus
[29]		Strut size	Scaffold stiffness and porosity
[30]		Topological geometry	Effective stiffness and permeability
[31]		Pore size	Effective stiffness and permeability
[4]		Strut size	Effective modulus and permeability, structural strength,
[32]		Pore size and location	Porosity distribution
[11,33]		Pore size	Porosity distribution
[34]		Pore shape	Overall stiffness
[35]		materials combination	Overall stiffness
[36]		Pore shape	Volume fraction subject to effective Young's modulus and pore size
[37]		Strut size	Compressive yield strength
[38]		Topological geometry	Prescribed bulk modulus and diffusivity
[39–42]	Time-independent bone growth	Strut size	Match bone elastic properties
[43]		Topological geometry	
[21]		Strut size	Reduce stress shielding
[22]		Strut size	Uniform stress distribution
[44,45]		Surface geometry	Desired wall shear stress
[13,14,16,17,46]	Time-dependent mechanobiological design	Strut size	Bone growth outcome
[15,25,47]		Topological geometry	
[48]		Pore size	
[49]		Pore size	Cell growth rate

time-independent and time-dependent design strategies.

Despite notable achievements in time-dependent design pertaining to bone scaffolds, there remains a dearth of efficient optimisation approaches for design of bulk scaffolds specifically tailored to address critical size defects. This challenge stems from the high computational cost incurred by the non-uniform bone ingrowth observed in each unit cell of the scaffolds. To tackle this critical challenge, we propose a dynamic mechanobiological optimisation strategy for design of functionally graded scaffolds here, which leverages machine learning (ML) techniques to enhance design efficiency significantly. In order to demonstrate the efficacy of the proposed method, we conduct a study on reconstruction of a critical size bone defect in a sheep mandible. We first prepared an *in-vitro* sheep mandible and fabricated an empirically designed scaffold, simulating the animal model for *in-vivo* experimental study. Then, a mechanical test was conducted on the sheep mandible-scaffold system, enabling to collect the pertinent data for validating the *in-silico* mandible-scaffold model. The *in-vitro* sheep mandible-scaffold system exhibited sufficient strength and an equivalent stiffness to that of the intact mandible in animal model. Finally, we compared various optimisation schemes, including a uniform design, a lateral gradient design, and a vertical gradient design, exploring their impact on bone regeneration outcomes.

The reminder paper is organised as follows. Section 2 presents the preparation of the sheep mandible, scaffold, and mechanical testing, followed by the mechanical validation of the finite element (FE) model for the sheep mandible-scaffold system. The proposed optimisation problem and the dynamic mechanobiological optimisation approach using ML techniques are also illustrated in detail in Section 2. The results are presented in Section 3, followed by discussions in Section 4. Finally, Section 5 draws some concluding remarks from this computational design study.

2. Materials and methods

2.1. Experimental design

2.1.1. Sheep mandible model and computed tomography (CT) scan

The sheep head was collected from a cadaveric sheep, as shown in Fig. 1(a). After collection, the head underwent scanning using the Siemens ARTIS Pheno, a robotic cone beam CT (CBCT) C-arm system manufactured by Siemens Healthcare GmbH in Germany. The scans were conducted following the manufacturer's standard protocol for a 16-slice Dyna Computed Tomography (DCT) scan with parameters of 0.5 deg/f, 20.0 ms pulse-width, and auto kV and mA settings. The acquired datasets were subjected to reconstruction using a Volume Rendering Technique (VRT) and primary examination using the Syngo VE10B workstation (Siemens Healthcare, GmbH, Germany). The resulting image datasets were exported in DICOM format with an isotropic voxel size of 0.36 mm. Subsequently, post-processing and image analyses were performed using the visualisation software 3dsMax (Autodesk, San Rafael, CA 94903, USA).

Following the CT scan of the sheep head, the skin covering the mandible was carefully removed using a surgical scalpel, blade, and forceps. The fascia and masseter muscles were then detached from their attachments, and the periosteum was elevated using a periosteal elevator. All muscle and skin attachments were meticulously cleared to enable manual downward displacement of the mandible and access to the temporomandibular joint (TMJ). The joint was freed with the aid of a pulling force. After removing the mandible from its anatomical location, any remaining muscle, fascia, periosteum, and nerve attachments were cleared using a scalpel, blade, and periosteal elevator.

Subsequently, a custom-designed 3D-printed resin surgical cutting guide was fitted to the left posterior part of the mandible at the horizontal and vertical ramus, as depicted in Fig. 1(b). The guide was secured using titanium screws that were drilled through the pre-arranged screw holes into the bone, ensuring a consistent osteotomy plane. A reciprocal saw was then utilised to perform the osteotomy dorsally at the vertical ramus and anteriorly beyond the last molar teeth. Once the osteotomy was completed, the guide was removed, and the SLS-printed Polyetherketone (PEK) mandibular scaffold implant was secured to the osteotomy sites using titanium

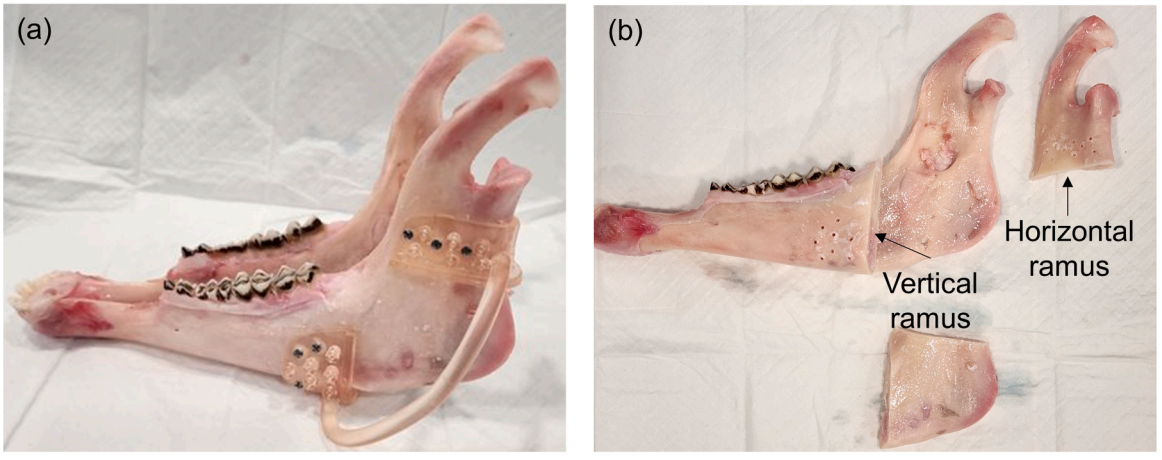

Fig. 1. Sheep mandible for the mechanical test. (a) The intact mandible from a cadaveric sheep. (b) The sheep mandible with a critical size defect.

screws through the same pre-drilled screw holes.

2.1.2. Scaffold preparation and fabrication

First, we used Materialise Mimics 22 software (Materialise NV, headquartered in Leuven, Belgium) for imaging segmentation and reconstruction of anatomical models of the head. Second, the resulting 3D models were exported to Autodesk 3dsMax, in which osteotomy planes were positioned to simulate the desired cut (Fig. 2(a)). Finally, we developed a sheep-specific implant by employing basic geometry tools and referencing the shape of the sheep mandible. This was achieved through the utilisation of spline projection, surface extrusion, and Boolean subtraction functions within Autodesk 3ds Max (Fig. 2(b)).

Triply Periodic Minimal Surface (TPMS) structures, specifically the Gyroid lattices, were utilised as the unit cell of the scaffold, with the unit-cell size of 4 mm and the wall thickness of 1 mm. The TPMS structure was integrated with the implant frame by performing a Boolean union in Autodesk 3dsMax (Fig. 2(c)). The final scaffold implant was then exported and printed using an EOS P810 (EOS Gmbh, Krailling, Germany) high-temperature Selective Laser Sintering (SLS) printer with the PEK material.

For the orientation and slicing of the implants into printing layers (thickness: 0.12 mm), Materialise Magics with an EOS building processor was employed. The y-axis of implants (Fig. 2(b)) was oriented parallel to the z-axis of the EOS P800, with the frame side facing downwards. This orientation was selected to prioritise surface accuracy at the bone-implant connection, ensure precise screw hole dimensions, and minimise the overall building height. Once the slicing process was completed, the layer files were loaded into PSW (V3.8) for build planning and execution. The implants were constructed using a custom laser exposure strategy that had been previously verified to enhance mechanical properties. The powder feedstock utilised was polyether ketone (PEK) under the trade name EOS PEEK HP3.

Following completion of the build process, the printed implants were allowed to cool using the default high-temperature cooldown routine until the temperature dropped below 60 °C. The implants were then carefully removed from the powder cake and cleaned visually using dry ice blasting. A ColdJet MicroClean Mk II machine was employed for the cleaning process, with a gauge pressure of 3 bar and a feed rate of 0.10 kg/min. Table 2 summarises the printing parameters used in the SLS fabrication of the PEK scaffold.

2.1.3. Mechanical tests

Mechanical assessment of the mandible-scaffold system was conducted using a TMA-WDW-10E Universal Testing Machine to evaluate the overall stiffness of the ovine mandibular bones, where the artificially created segmental defects were bridged by PEK-based scaffold constructs. As shown in Fig. 3, a custom metal jig was manufactured and secured to the lower crosshead. This jig consists of the two rigid metal horizontal platforms positioned on an adjustable substrate designed to accommodate the various geometries of sheep mandibles. The entire jig was affixed to the lower crosshead and moved along with it. Two nylon straps were employed to securely fasten both sides of the mandible to the upper load cells, ensuring the controlled displacement in the vertical direction at a constant rate of 5 mm/min. The upper platform maintained firm contact with the condyle, applying a downward force to the specimen, while the movement of the incisor teeth was restricted by the lower horizontal platform. This unique testing setup generated a biting force that was transferred to the scaffold-host bone structure, somewhat similar to the in vivo loading scenario.

The mechanical tests were carried out under a displacement-controlled load, continuing until the vertical displacement of the loading cell reached 5.9 mm prior to the fracture failure of the PEK scaffold, which ensured a nearly linear deformation of the specimen. Note that for the mechanical test analysis, the initial linear segment of the force-displacement curve was considered to represent the forces required to fully stretch the nylon straps. The second linear segment of the test curve was considered indicative of the specimen's modulus and stiffness.

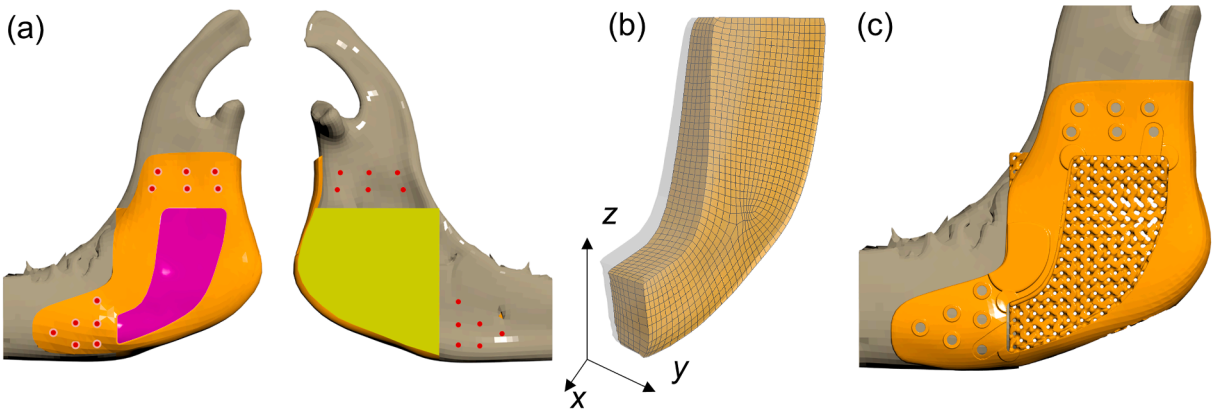

Fig. 2. The preparation of a customised scaffold for the sheep mandible. (a) The critical size defect in the sheep mandible model. (b) The homogenised scaffold area in the sheep mandible model. (c) The scaffold filled with Gyroid type unit cells.

Table 2
SLS PEK 3D Printing Parameters.

Printing parameters	value
Layer thickness	0.12 mm
Build area configuration	230 mm x 350 mm
Base layers	2.5 + 6 mm
Top layers	3 mm
Process chamber temperature	365 °C
Building platform temperature	336 °C
Exchangeable frame temperature	343 °C
Post sintering time	12 s
Beam offset	0.42 mm
Laser exposure set	Custom
Cooldown	High temp cooldown

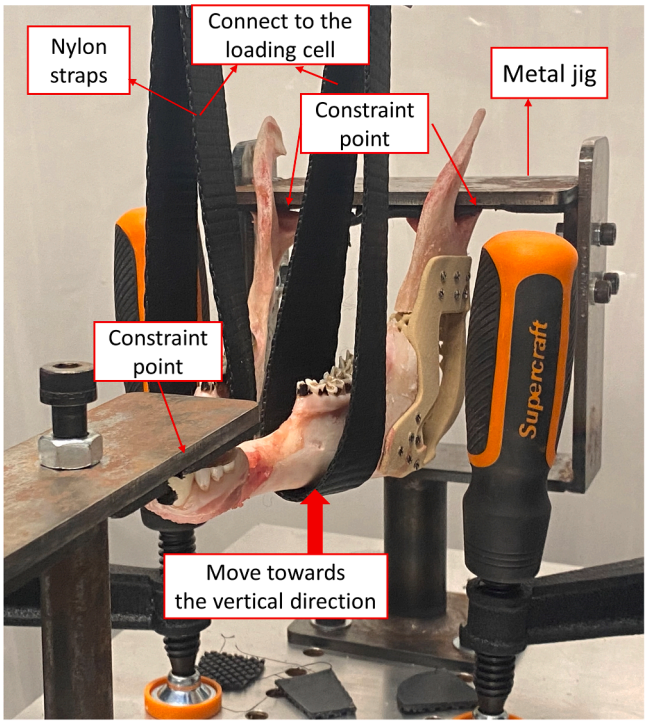

Fig. 3. The setup of the mechanical test of the sheep mandible-scaffold system.

2.2. Numerical model simulating the mechanical test

2.2.1. Finite element model

In this study, a CT image-based finite element (FE) modelling approach was applied to simulate the mechanical test result, aimed to validate the accuracy of the established FE model that was used for subsequent design optimisation study. Fig. 4(a) illustrates the simulated FE model, which includes the sheep mandible, scaffold, and screws. The sheep mandible was segmented and reconstructed from the CT scans and meshed using linear tetrahedral elements in ScanIP (Synopsys Simpleware, Mountain View, CA), containing 1,556,549 elements with a total of 1,049,280 degrees of freedom (DOFs). The scaffold was also meshed using linear tetrahedral elements, resulting in additional 815,442 elements and 636,606 DOFs. The screws were represented by rigid elements to connect the scaffold with the sheep mandible.

In the FE model, all the materials were assumed to be isotropic and linear elastic. Young's modulus of mandibular bone was considered heterogeneous at different locations. To achieve this, we adopted a CT-pixel based algorithm to determine the bone density of the cortical bone [50]. A power law model $E_{cor} = 5218\rho^{2.29}$ MPa was employed to determine site-dependent Young's modulus with respect to different bone density values [2], as illustrated in Fig. 4(b). The maximum Young's modulus of cortical bone $\overline{E}_{cor}$ was assumed to be 15,700 MPa [2]. The trabecular bone was assumed homogeneous with an average Young's modulus $\overline{E}_{tr}$ of 300 MPa [51]. The distinction of the material properties between teeth and cortical bone was ignored as the difference in predicted biomechanics can be ignored according to the previous study [51]. Young's modulus of the scaffold base material PEK ($\overline{E}_{PEK}$) was given as 2,400 MPa [52]. A Poisson's ratio ($\overline{\mu}$) of 0.3 was used for all bone tissues and the scaffold [51].

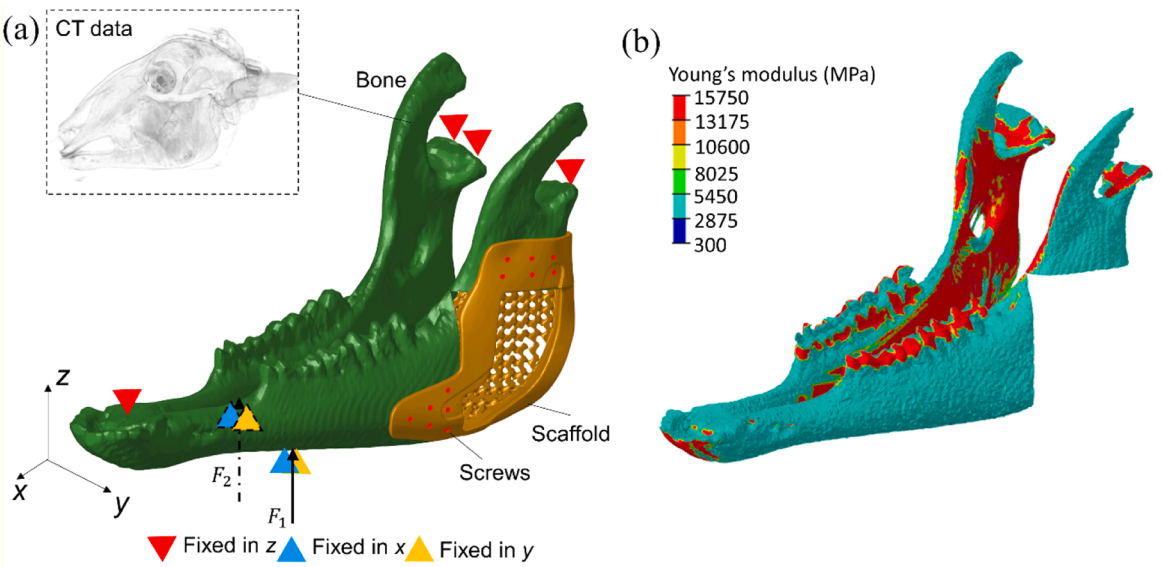

Fig. 4. Finite element (FE) model for simulating the mechanical test of the sheep mandible-scaffold system. (a) The FE model with loading and boundary conditions; (b) The distribution of Young's modulus of cortical bone derived from computed tomography (CT) data.

2.2.2. *Loading and boundary conditions*

In the FE model, the load and boundary conditions were prescribed to match those used in the actual mechanical test, as illustrated in Fig. 4. For simulating the fixation positions, the sheep condylar region and the premolar teeth area were assumed to be fixed in the z-direction, representing their immobilisation. To replicate the loading conditions, two maximum displacement-controlled loads (F_1 and F_2) were set to be 5.9 mm in z-direction with x and y DOFs constrained (Fig. 4). The corresponding forces were then employed to calculate the stiffness of the sheep mandible-scaffold system.

2.3. *Dynamic mechanobiological model for tissue growth*

This study employed a time-dependent dynamic mechanobiological model previously developed in [17,50] to simulate bone growth into scaffolds. In this model, the scaffold composed of porous unit cells is treated as a solid and homogenised media at a

Table 3
The parameters in the dynamic bone growth model.

Parameters	Description	Values	Units	Reference
$\overline{\rho}$	Maximum bone density	1.62	g/cm^3	[57]
$\underline{\rho}$	Minimum bone density	0.05	g/cm^3	[55]
$\overline{E}_{cor}$	Maximum Young's modulus of cortical bone	15,700	MPa	[57]
$\overline{E}_{tr}$	Young's modulus of trabecular bone	300	MPa	[51]
$\overline{E}_{PEK}$	Young's modulus of PEK scaffold	2,400	MPa	[52]
$\overline{\mu}$	Poisson's ratio	0.3	–	[51]
Δt	Fictitious time for each time-step	72	h	–
S_E	Empirical constant of effective scaffold specific area	0.6	–	[16]
c_s	Empirical constant of the sensitivity to mechanical stimuli	0.02	μm/MPa	[16]
$\overline{\psi}$	Reference stimulus level	600	MPa/72h	[16]
l	Lazy zone	150	MPa/72h	[16]
p	Power value of the p-norm function	4	–	[58]
$\overline{\kappa}$	Ersatz diffusivity	0.001	mm^2/72h	[16]
$\overline{B}$	Maximum diffusivity of bone	1,200	mm^2/72h	[55]
$\underline{\mathbf{D}}$	Lower bound of scaffold rods	0.3	mm	–
$\overline{\mathbf{D}}$	Upper bound of scaffold rods	0.75	mm	–

macroscopic level, in which each representative volume element (RVE) characterises a single unit cell with specific structures at a microscopic level. In this section, we briefly illustrate the dynamic mechanobiological model, followed by detailed explanation of the coupled dynamic mass diffusion analysis performed by the FE approach.

2.3.1. Dynamic bone growth modelling

The bone density is updated on an element basis in every time step, in which each RVE is associated with a bone density which is calculated at the centroid numerically. It should be noted that each RVE encapsulates both the microstructure of the scaffold and the newly formed bony tissue that is assumed to be uniform within a specific RVE [17,50].

The Euler forward algorithm is employed to update the bone density at time step $n+1$ for the r^{th} RVE expressed as,

$$\rho_r^{(n+1)} = \min\left(\overline{\rho},\ \rho_r^{(n)} + \dot{\rho}_r^{(n)}\Delta t\right), \tag{1}$$

where $r \in [1, R]$ with R denoting the total number of RVEs in the scaffold. $\rho_r^{(n+1)}$ and $\rho_r^{(n)}$ denote the bone density at time step $n+1$ and n, respectively. $\dot{\rho}_r^{(n)}$ represents the change rate of bone density at time step n. $\overline{\rho}$ is the allowed maximum bone density, with its value illustrated in Table 3. Δt is a fictitious time here.

Eq. (1) relies on the derivation of $\dot{\rho}_r^{(n)}$ at time step n, which can be calculated as,

$$\dot{\rho}_r^{(n)} = S_E S_r^{(n)} \dot{\varphi}_r^{(n)} \overline{\rho}, \tag{2}$$

where S_E is an empirical constant determining the specific surface area favouring bone growth. $S_r^{(n)}$ represents the specific surface area of the r^{th} RVE at time step n, which is calculated numerically using a geometric projection method to be explained in Section 2.4. $\dot{\varphi}_r^{(n)}$ denotes a deposition rate of bone in the r^{th} RVE at time step n, expressed as,

$$\dot{\varphi}_r^{(n)} = \begin{cases} c_s \lambda_r \left(\psi_r^{(n)} - \overline{\psi} - l\right), & \text{if } \psi_r^{(n)} - \overline{\psi} > l \\ 0, & \text{otherwise} \end{cases}, \tag{3}$$

where c_s is an empirical constant as given in Table 3. λ_r denotes the normalised concentration of osteoblasts with a maximum concentration of 100 %, which is calculated by applying the Fick's law, detailed in Section 2.3.2. $\overline{\psi}$ is a reference stimulus level, and l is the lazy zone around the reference stimulus level. $\psi_r^{(n)}$ stands for the mechanical stimulus applied in the r^{th} RVE at time step n, calculated as,

$$\psi_r^{(n)} = \left[\frac{\overline{\rho}}{\rho_r^{(n)}}\right]^2 \left[\sum_{i=1}^{I} m_i \left(\widetilde{\sigma}_{r,i}^{(n)}\right)^p\right]^{\frac{1}{p}} \tag{4}$$

where m_i denotes the number of loading cycles for load case $i \in [1, I]$. $\widetilde{\sigma}_{r,i}^{(n)}$ is the effective stress in the r^{th} RVE at time step n corresponding to load case i. It is noted that a p-norm function is employed in Eq. (4) to approximate the highest effective stress $\widetilde{\sigma}_{r,i}^{(n)}$ of different load cases.

In order to prevent a zero denominator in Eq. (4), a minimum bone density $\underline{\rho}$ is assumed to be uniformly distributed at the initial time step, representing early-phase osseointegration and tissue proliferation matter [53,54]. The effective stress $\widetilde{\sigma}_{r,i}^{(n)}$ in Eq. (4) is calculated as,

$$\widetilde{\sigma}_{r,i}^{(n)} = \sqrt{2E_r^{(n)} W_{r,i}^{(n)}}, \tag{5}$$

where $W_{r,i}^{(n)}$ is the strain energy of the r^{th} RVE at time step n for load case i. $E_r^{(n)}$ denotes the average Young's modulus of the r^{th} RVE that contains both scaffold microstructure and newly formed bone at time step n, expressed as [55],

$$E_r^{(n)} = C_{4444}\left(\frac{3C_{1122} + 2C_{4444}}{C_{1122} + C_{4444}}\right), \tag{6}$$

where C_{1122}, C_{4444} denote the elastic tensor components obtained from the homogenisation analysis as [56],

$$C_{qjkg} = \frac{1}{|\Omega^r|}\int_{\Omega^r} D_{qjzf}\left[\overline{\epsilon}_{zf}^{(kg)} - \widetilde{\epsilon}_{zf}^{(kg)}\right] d\Omega, \tag{7}$$

where $\overline{\epsilon}_{zf}^{(kg)}$ is the characteristic strain tensors, $\widetilde{\epsilon}_{zf}^{(kg)}$ is the locally varying micro-strain tensors induced by $\overline{\epsilon}_{zf}^{(kg)}$. D_{qjzf} denotes either the elastic tensor of scaffold architectural materials or newly formed bone at time step n. Ω^r represents the total volume of the r^{th} RVE.

2.3.2. Dynamic mass diffusion modelling

The concentration of osteoblasts λ_r in the r^{th} RVE can be determined by the Fick's second law of diffusion, the strong form of which

is expressed as,

$$\begin{cases} -\dfrac{\mathrm{d}\lambda}{\mathrm{d}t} + \boldsymbol{\kappa}\nabla\cdot(\nabla\lambda) = 0, \ \text{in } \Omega_s \\ \lambda = \overline{\lambda}, \ \text{on } \Gamma_s \end{cases}, \tag{8}$$

where λ is the normalised concentration of osteoblasts in the homogenised scaffold region Ω_s. t is the time, $\boldsymbol{\kappa}$ denotes the diffusivity tensor obtained from the homogenisation analysis. Γ_s denotes the concentration boundary given as a specific concentration of osteoblasts $\overline{\lambda}$. In this study, Γ_s represents the scaffold surfaces that contact with host cortical bone ($\overline{\lambda} = 100$ %).

The weak form of Eq. (8) can be obtained by introducing a virtual concentration $\delta\lambda$, expressed as,

$$\int_{\Omega_s} -\frac{\mathrm{d}\lambda}{\mathrm{d}t}\ \delta\lambda \mathrm{d}\Omega_s + \int_{\Omega_s} \boldsymbol{\kappa}\delta\lambda\nabla\cdot\nabla(\delta\lambda)\mathrm{d}\Omega_s = 0 \tag{9}$$

Using the integration-by-parts theorem, the second term of Eq. (9) can be expressed as,

$$\int_{\Omega_s} \boldsymbol{\kappa}\delta\lambda\nabla\cdot\nabla(\delta\lambda)\mathrm{d}\Omega_s = -\int_{\Omega_s} \boldsymbol{\kappa}\nabla\delta\lambda\cdot\nabla\lambda\ \mathrm{d}\Omega_s + \int \boldsymbol{\kappa}\delta\lambda\cdot(\nabla\lambda\cdot\mathbf{n})\mathrm{d}\Gamma, \tag{10}$$

where Γ denotes the external boundary with $\nabla\lambda\cdot\mathbf{n} = 0$. Therefore, Eq. (9) is rewritten as,

$$\int_{\Omega_s} \frac{\mathrm{d}\lambda}{\mathrm{d}t}\ \delta\lambda \mathrm{d}\Omega_s + \int_{\Omega_s} \boldsymbol{\kappa}\nabla\delta\lambda\cdot\nabla\lambda\ \mathrm{d}\Omega_s = 0. \tag{11}$$

Using the FE method, the weak form of Eq. (11) can be finally discretised into,

$$\mathbf{M}\dot{\boldsymbol{\lambda}} + \boldsymbol{K}\boldsymbol{\lambda} = 0 \tag{12}$$

where $\boldsymbol{\lambda}$ and $\dot{\boldsymbol{\lambda}}$ are the global vectors of osteoblast concentration and its time derivative. $\mathbf{M}$ and $\mathbf{K}$ are the global concentration capacity matrix and concentration conduction matrix, assembled respectively as,

$$\mathbf{M} = \cup_{r=1}^{R} \int_{\Omega_s} \mathbf{N}_r^{\mathrm{T}}\mathbf{N}_r \mathrm{d}\Omega_s, \tag{13}$$

$$\mathbf{K} = \cup_{r=1}^{R} \int_{\Omega_s} \mathbf{B}_r^{\mathrm{T}}\boldsymbol{\kappa}_r^{(n)}\mathbf{B}_r \mathrm{d}\Omega_s, \tag{14}$$

where $\mathbf{N}_r$ and $\mathbf{B}_r$ are the shape function and its spatial derivative matrix of the r^{th} RVE in the scaffold.

Note that $\boldsymbol{\kappa}_r^{(n)}$ is the homogenised diffusivity tensor of the r^{th} RVE at time step n, calculated as [16],

$$\boldsymbol{\kappa}_r^{(n)} = \frac{1}{|\Omega^r|}\int_{\Omega^r} \kappa\left(\boldsymbol{\chi}^0 - \boldsymbol{\chi}\right) d\Omega, \tag{15}$$

where κ is either the isotropic diffusivity of newly formed bone estimated according to the permeability of bone or an ersatz diffusivity tensor $\overline{\kappa}$ of scaffold base materials with a non-zero but very small value to prevent numerical illness. $\boldsymbol{\chi}^0$ and $\boldsymbol{\chi}$ are the unit concentration gradient field and the induced concentration gradient field, respectively. It is noted that the diffusivity tensor of newly formed bone is updated in the dynamic mass diffusion analysis with a maximum diffusivity of 1,200 $\mathrm{mm}^2/72\mathrm{h}$ [55].

To discretise Eq. (12) in the temporal domain, $\dot{\boldsymbol{\lambda}}$ and $\boldsymbol{\lambda}$ are approximated with respect to time step $n-1+\theta$, respectively as,

$$\dot{\boldsymbol{\lambda}}_{n-1+\theta} = \frac{\boldsymbol{\lambda}_n - \boldsymbol{\lambda}_{n-1}}{\Delta t}, \tag{16}$$

$$\boldsymbol{\lambda}_{n-1+\theta} = \theta\boldsymbol{\lambda}_n + (1-\theta)\boldsymbol{\lambda}_{n-1}. \tag{17}$$

Thus, Eq. (12) can be written as,

$$\left(\frac{\mathbf{M}}{\Delta t} + \theta\mathbf{K}\right)\boldsymbol{\lambda}_n = \left[\frac{\mathbf{M}}{\Delta t} - (1-\theta)\mathbf{K}\right]\boldsymbol{\lambda}_{n-1}, \tag{18}$$

where Δt is fictitious time for each time step (as previously defined in Section 2.3.1), θ is a constant value controlling which finite difference method is used to calculate $\boldsymbol{\lambda}_n$. If $\theta = 0$, the forward difference method is employed; If $\theta = 1$, the backward difference method is employed. In this study, the Crank-Nicolson method is used with $\theta = 1/2$ as it can achieve the second-order accuracy

concerning the temporal domain [59].

2.4. Design optimisation of scaffold

2.4.1. Optimisation model

It can be noted that the dynamic bone growth model introduced in Section 2.3 relies on a homogenised scaffold model at the macroscopic level and the homogenisation analyses at the microscopic level. Therefore, we modified the FE model by replacing the original mono-scale scaffold with a homogenised scaffold (Fig. 5) for design optimisation. Furthermore, the loading and boundary conditions of the sheep mandible-scaffold system were prescribed to simulate the actual clenching action that the system would encounter *in vivo*. As illustrated in Fig. 5(a), all teeth, including incisors, molars and premolars, were fixed in z-direction to simulate occlusion. The sheep condylar was assumed to be fully fixed in the mandibular fossa. Various muscle groups were applied to the intact side of the sheep mandible, which encompassed the superficial masseter (SM), deep masseter (DM), medial temporalis (MT), posterior temporalis (PT), medial pterygoid (MPt), inferior lateral pterygoid (LPt), and temporalis muscle (TEMP). Table 4 summarises the maximum force and direction cosine associated with each muscle applied in the FE model for optimisation followed by a previous study [51].

2.4.2. Definition of optimisation problem

In this study, the objective is to maximise newly formed bone mass in the scaffold subject to a stiffness constraint that ensures sufficient support after implantation, which can be mathematically expressed as,

$$\begin{cases} \max \mathscr{L} = \sum_{r=1}^{R} V_r \rho_r^N \\ \text{subject to } Y \geq Y^* \\ \underline{\mathbf{D}} \leq \mathbf{D} \leq \overline{\mathbf{D}} \end{cases}, \tag{19}$$

where $\mathscr{L}$ represents the total newly formed bone mass within the scaffold, V_r is the volume of the r^{th} RVE, ρ_r^N is the bone density of the r^{th} RVE at the final time stage concerned N. In this study, the time increment Δt was assumed to be 72 h (3 days), and N was set to be 20, representing the dynamic bone growth over a 60-day period in the sheep mandible. Y denotes the stiffness of the whole sheep mandibular scaffold, and Y^* is the stiffness based on the intact sheep mandible subject to the load condition as defined in Section 2.4.1,

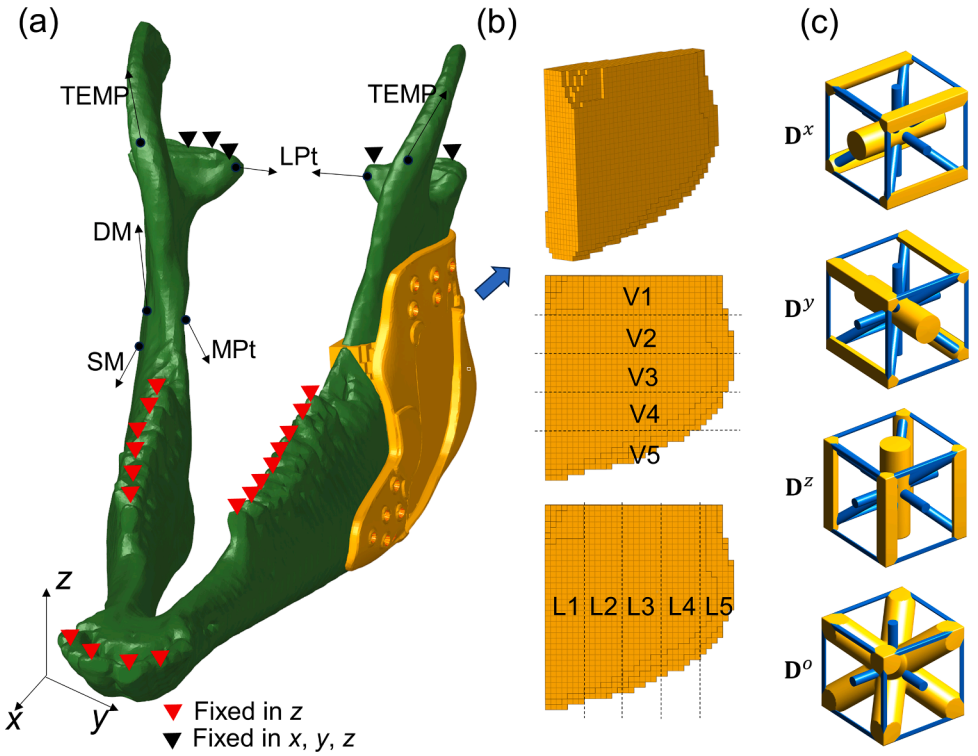

Fig. 5. The finite element (FE) model for the design optimisation of scaffold structure. (a) The loading and boundary conditions. (b) The homogenised scaffold with vertical (V1-V5) and lateral (L1-L5) gradient areas. (c) The isotruss structure of unit cells with the design variables $\mathbf{D}^x$, $\mathbf{D}^y$, $\mathbf{D}^z$, $\mathbf{D}^o$ controlling the diameter of rods.

Table 4
Sheep mandible muscle's maximum force and direction cosines [51].

Sheep mandible muscle	Maximum force	Direction cosine			
		X	Y		Z
			Right	Right	
Superficial masseter	292.5	0.840	−0.054	0.054	0.539
Deep Masseter	136.4	0.248	−0.539	0.539	0.805
Temporalis	165.9	−0.840	.036	−0.036	0.541
Medial pterygoid	162.7	0.083	0.186	−0.186	0.979
Lateral pterygoid	62.8	0.716	0.400	−0.400	0.574

which was considered in the optimisation to avoid potential failure and/or malfunction.

In Eq. (19), $\mathbf{D}$ denotes the vector of design variables that control the microstructure of RVEs in the scaffold. $\underline{\mathbf{D}}$ and $\overline{\mathbf{D}}$ represent their lower bound and upper bound, respectively. An isotruss lattice was employed as the base structure (Fig. 5(c)). Here the isotruss lattice consists of 19 rods, and the diameter of each rod can be controlled using a geometric projection method [60], efficiently facilitating the construction of the lattice. In this study, the 19 rods in the isotruss lattice were divided into four groups for optimisation: group x with design variable vector $\mathbf{D}^x$, group y with design variable vector $\mathbf{D}^y$, group z with design variable vector $\mathbf{D}^z$, and group diagonal with design variable vector $\mathbf{D}^o$. Fig. 5(c) highlights the rods belonging to each group in yellow.

Three optimisation schemes were considered here to compare with an empirical design. In the empirical design, all the isotruss struts were set as 0.45 mm to meet the stiffness constraint Y^*. The first scheme involved an optimisation based on a uniform design, in which all RVE microstructures were identical. Thus, the first scheme of uniform RVE has four design variables $\mathbf{D}_u = [D_u^x, D_u^y, D_u^z, D_u^o]$. The second scheme was a vertical gradient design, where the scaffold was divided into five gradient regions $V1$, $V2$, $V3$, $V4$, and $V5$, as shown in Fig. 5(b). Each unit cell in the vertical gradient design has four design variables, resulting in a total of 20 design variables $\mathbf{D}_V = \{D_{V,\varsigma}^x, D_{V,\varsigma}^y, D_{V,\varsigma}^z, D_{V,\varsigma}^o \big| \varsigma = 1, 2, 3, 4, 5\}$. The third scheme was a lateral gradient design, as shown in Fig. 5(b). In the lateral gradient design, the scaffold was divided into five domains ($L1$, $L2$,$L3$, $L4$, and $L5$) in the lateral direction with 20 design variables $\mathbf{D}_L = \{D_{L,\varsigma}^x, D_{L,\varsigma}^y, D_{L,\varsigma}^z, D_{L,\varsigma}^o \big| \varsigma = 1, 2, 3, 4, 5\}$ in total. The lower bound of the rod diameters $\underline{\mathbf{D}}$ was set to be 0.3 mm due to the resolution constraint of the PEK printing technique [61], and the upper bound $\overline{\mathbf{D}}$ was set to be 0.75 mm to prevent non-porous lattices in the scaffold.

2.4.3. Machine learning (ML) methods

The dynamic mechanobiological model relies on the homogenisation analysis to determine the effective elastic tensor and diffusivity tensor at the micro-scale level. It is noted that the newly formed bone densities in each RVE are different due to the non-uniform distribution of mechanical stimuli and osteoblast mass concentration [16]. Therefore, the FE-based homogenisation analyses must be performed on every RVE, rendering prohibitively high computational cost.

To tackle this computational burden, we implemented two neural networks (namely, NN-1 and NN-2) to predict the effective elastic tensor and diffusivity tensor, respectively. In NN-1, the input layer consists of five inputs representing the design variables D^x, D^y, D^z, D^o and bone density $\rho^{(n)}$. The output layer of NN-1 comprises nine independent components of the homogenised (effective) elastic tensor. Similarly, NN-2 shares the same input layer as NN-1, but its output layer consists of three independent components of homogenised (effective) diffusivity tensor.

To determine the optimal performance for accurately predicting the effective elastic and diffusivity tensors, we tested with various configurations for the number of neurons in the hidden layer of NN-1 and NN-2. Specifically, we evaluated the performance of the models using 10, 20, 30, 50, 100, and 150 neurons in the hidden layer. The ground-truth data contained 3000 homogenisation samples generated using the Latin hypercube sampling method [62] and the geometric projection approach [63], with sample sizes ranging from 0.3 to 0.75 mm. The effective elastic and diffusivity tensors were computed through the FE-based homogenisation analyses as defined in Eqs. (7) and (15), respectively. Note that the computational process for obtaining the ground-truth data required approximately 16.6 h and was parallelly distributed across six desktops (RAM 128 GB and CPU Intel(R) Core (TM) i7–7820X). Moreover, the ground-truth data were divided into training (70 %), validation (15 %), and testing (15 %) datasets. The accuracy of neural networks, featuring varying numbers of neurons, was assessed using mean square errors between the predicted and calculated effective tensors.

2.4.4. Optimisation method

To solve the optimisation problem defined in Eq. (19), a combination of a genetic algorithm [64] and a neural network (NN-3) was employed to search the quasi-global optima in for the different optimisation schemes (Fig. 6(a)). The first step involved in building NN-3, which was trained to predict the objective function $\mathscr{S}$ (i.e. total bone density) and the constraint Y (mandible-scaffold stiffness) function based upon different design variables $\mathbf{D}$ in various design schemes. For the uniform, vertical, and lateral gradient designs, we generated 1000, 3000, and 3000 optimisation samples, respectively, using the Latin hypercube sampling method [62]. These optimisation samples were generated from the dynamic bone-growth model using NN-1 and NN-2 (Fig. 6(b)). The regression values between the predicted and FE-calculated objective and constraint were used to demonstrate the effectiveness of NN-3. In the second step,

the genetic algorithm was employed to search the optimum design variables for the uniform, vertical, and lateral gradient designs, respectively. The objective and constraint functions were efficiently evaluated using NN-3.

Fig. 6(b) further illustrates the process of generating the optimisation samples for training NN-3 using the proposed ML-based dynamic time-dependent bone-growth model. First, the design variables and initial bone density were input to NN-1 and NN-2 to predict the homogenised elastic tensor and diffusivity tensor of each RVE, respectively. Second, the FE analysis was performed based on the homogenised elastic tensors to determine the mechanical stimuli at each RVE. Concurrently, mass diffusion analysis was conducted to calculate the concentration at each RVE. Finally, the bone density of each RVE was updated using Eq. (1). The above procedure was repeated until the desired growth time T (60 days) was achieved.

3. Results

3.1. Validation of the finite element model

Table 5 presents the stiffness values of the constructed sheep mandible-scaffold system obtained from the in-house mechanical tests and the FE simulation. The FE analysis yielded a stiffness value of 43.15 N/m, closely matching the mean stiffness of 45.07 N /m obtained from the mechanical tests, with a fairly low relative error of 4.26 %.

Fig. 7(a) illustrates the distribution of the vertical displacement in the FE results. It is evident that the critical size defect treated by the scaffold exhibits significant vertical deformation compared to the intact half side. This observation indicates that the stiffness of the critical size area is lower than that of the intact mandible, as Young's modulus of the scaffold base material (PEK) is substantially lower (2,400 MPa) than that of the cortical bone (15,700 MPa). Fig. 7(b) and (c) also illustrate the distribution of von Mises equivalent strain and von Mise equivalent stress within the sheep mandible-scaffold system. Concentrations of the strain and stress can be observed around the left upper re-entrant corner of the scaffold, while the sheep mandible experiences lower magnitudes of strain and stress than the scaffold. From the FE analysis, the stiffness of the scaffold plays a crucial role in determining the overall stiffness of the constructed mandible-scaffold system.

3.2. Validation of neural network models

To assess the modelling accuracy of NN-1 and NN-2, we calculated the mean square errors (MSEs) based on the training and testing homogenisation samples. When 10 neurons were employed in the hidden layer, the structure of the NNs might be too simple to output accurate tensors after training. Once the hidden neurons increased to 20, we could observe some drop of output errors attributed to the

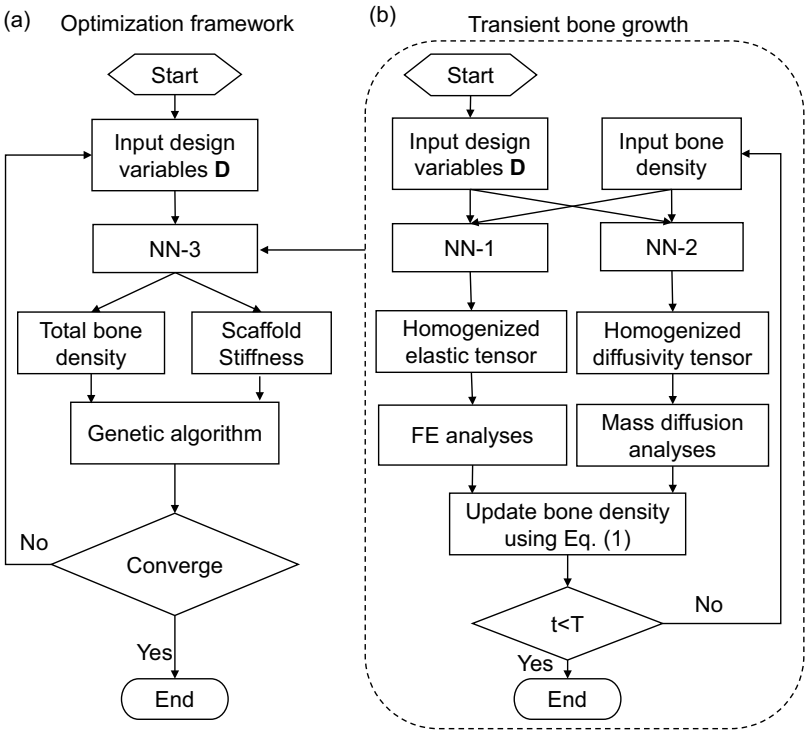

Fig. 6. The flowchart of the proposed machine learning based mechanobiological approach for the dynamic design of customised scaffolds. (a) The optimisation framework. (b) The dynamic bone growth model using machine learning techniques.

Table 5
Comparison of stiffness obtained from the mechanical test and finite element analysis.

Performance	Mechanical tests			Finite element analysis	Error
	Test 1	Test 2	Test 3		
Stiffness N/m	46.86	44.22	44.12	43.15	4.26 %

increased complexity of the neural networks for better modelling this sophisticated process. In Fig. 8(a), the minimum MSE for the training data was found to be 8.93×10^{-6}, which occurred when NN-1 had 100 neurons in the hidden layer. Similarly, the minimum MSE for the testing data was also observed with NN-1 comprising 100 neurons in the hidden layer, with a slightly higher value of 1.17×10^{-5} compared to the training data. As a result, we selected NN-1 consisting of 100 neurons in the hidden layer to output the effective homogenised elastic tensor.

Fig. 8(b) compares the MSEs of NN-2 tested on the hidden layers with 10, 20, 30, 50,100, and 150 neurons. The minimum MSE for the training data was found to occur with NN-2 comprising 30 neurons, with a value of 3.24×10^{-6}, marginally higher than its MSE for the testing data 3.15×10^{-6}. Additionally, it can be observed in Fig. 8(b) that the MSEs decrease when the number of neurons increases from 10 to 30. After that, the MSEs exhibit a slight rise with further increases in the number of neurons. To avoid overfitting, we selected NN-2 consisting of 30 neurons to predict the effective diffusivity tensor with reasonably high accuracy.

Fig. 9 illustrates the regression values of NN-3 for the optimisation of the uniform, vertical and lateral gradient schemes, in which the regression analyses were performed on all the data (training, validation and testing) and test data, respectively. NN-3 for the uniform design (NN-3-U) was trained with ten neurons in the hidden layer, resulting in a significantly higher regression value with 0.99945 on all the data and 0.99851 on the test data. NN-3 for the vertical gradient (NN-3-V) and lateral gradient designs (NN-3-L) were trained with 20 neurons as the number of inputs is higher than that of the uniform design (20 vs 4). Apparently, all the NN-3 models achieved substantially high regression values (greater than 0.996) on the test data, demonstrating that NN-3-U, NN-3-V, and NN-3-L can be used for the optimisation studies.

3.3. Optimisation results

The optimised diameters obtained from these three design schemes are summarised in Table 6. In order to demonstrate the effectiveness of the proposed optimisation framework, we compared the three design schemes with the empirical design.

For the uniform design, the struts oriented towards the y-direction were reinforced, while the strut sizes in the x and z-directions were reduced in comparison with those in the empirical design. In the vertical gradient design, the strut sizes in different gradient areas show significant differences. A similar trend can also be observed in the lateral gradient design, where the unit cells in different gradient areas were rationally tailored to optimise bone growth outcomes over the 60-day treatment period while still satisfying the stiffness constraint at the same time. Fig. 10(b)-(e) provides the details of the optimised unit cells in the empirical design, the uniform design, the vertical gradient design, and the lateral gradient design.

It is noted that there might be small errors in the total bone density after 60 days obtained from NN-3 compared to the actual response from the FE analyses. Table 6 compares the predicted total bone density obtained from NN-3 and the actual bone density obtained from FE analyses with the optimised strut diameters. For the uniform design, the total bone density predicted by NN-3 is 3086.64 g/cm^3, which is 1.59 % higher than the actual modelling value from the FE analyses (3038.41 g/cm^3). In the case of the vertical gradient design, the total bone density predicted by NN-3 is 3305.17 g/cm^3, which is 3.02 % higher than the value from the FE analyses (3208.04 g/cm^3). For the lateral gradient design, the total bone density is 3487.7 g/cm^3, 1.20 % lower than the value from FE analyses (3529.50 g/cm^3). Despite the minor prediction errors of NN-3, the proposed design framework exhibited fairly accurate computational results, which was validated through the FE analyses on the optimised isotruss unit cells.

Fig. 10(a) compares the histories of bone growth within the four different scaffold configurations over 60 days. From the beginning (day 3), it can be clearly seen that the total bone density from the lateral gradient design is notably higher than the other three designs. Although the differences in the total bone density among the other three designs are relatively negligible in the early days, the advantages of the optimal designs become more evident from day 9, where both the uniform design and vertical gradient design start outperforming the empirical design, exhibiting an increasing difference in bone density over time. By day 24, the bone growth outcome within the vertical gradient design is found to surpasse that of the uniform design, showing superior performance in terms of bone density and formation.

Fig. 11 illustrates the distribution of newly formed bone within the scaffolds obtained from the different designs, focusing on the areas with a neobone density higher than 0.35 g/cm^3. Of all the designs, a similar trend in bone growth is observed, with bone formation initiating from the interfaces between the scaffold and host bone, attributed to the high concentrations of osteoblasts at these locations. Moreover, the role of mechanical stimuli in influencing bone growth is evident, leading to distinct outcomes among the various designs. The results reveal that the optimised uniform design outperformed the empirical design in terms of bone growth, demonstrating the effectiveness of the proposed optimisation framework.

4. Discussion

Several literature studies have dedicated their efforts to the area of mechanobiological design for bone scaffolds [13,15,17,25,26,

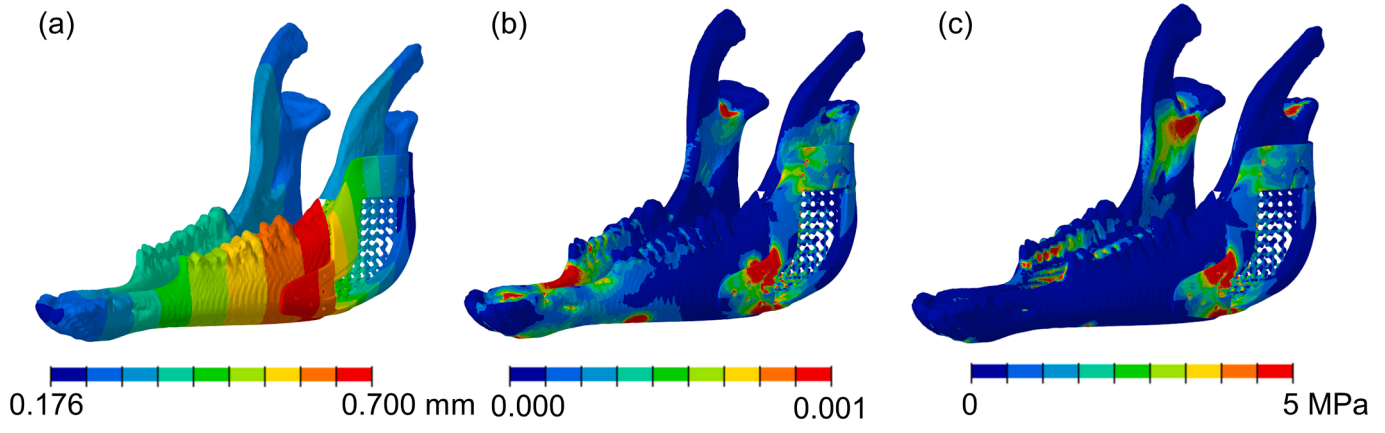

Fig. 7. The results of the FE analysis based on the simulated mechanical tests. (a) The vertical displacement contour. (b) The von Mises equivalent strain contour. (c) The von Mises equivalent stress contour.

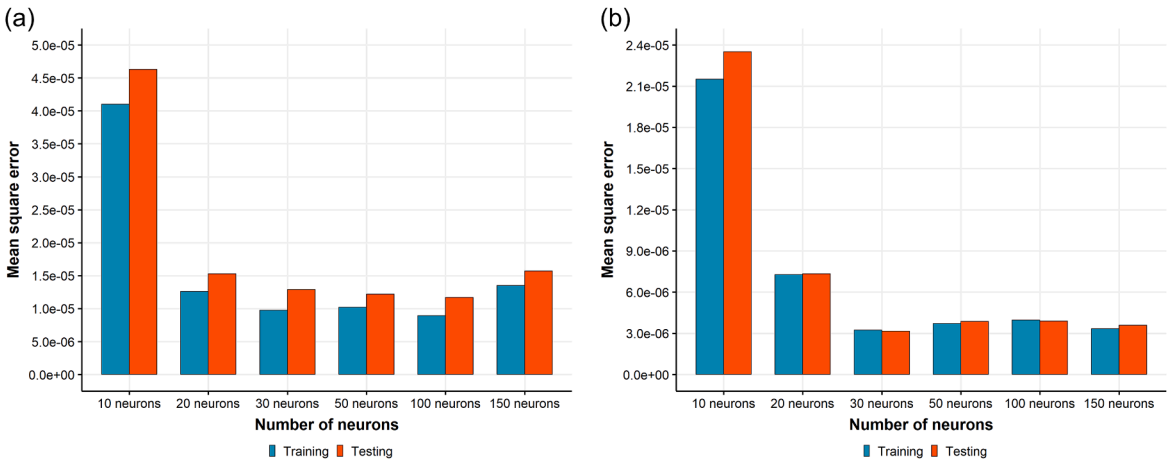

Fig. 8. Mean square errors (MSE) for the training and testing data with different numbers of neurons in the hidden layers. (a) Neural network 1 ((NN-1) for predicting effective elastic tensors. (b) Neural network two (NN-2) for predicting effective diffusivity tensors.

65]. Their findings highlighted the importance of considering long-term bone regeneration outcomes as one of the critical criteria in the design process. Nevertheless, the conventional FE-based homogenisation process, requiring repeated calculation on each RVE at every time step, often results in a prohibitively high computational cost for the dynamic time-dependent mechanobiological model. As an example, conducting FE-based homogenisation for the effective elastic and mass diffusivity tensors on a desktop (CPU: Intel i7–7820X, RAM: 128 GB) for an isotruss unit cell takes approximately 2 min in total. Extrapolating such computational time to the bulk scaffold (8502 RVEs) utilised in this study would require an impractical total of 340,080 min (equivalent to approximately 236.2 days) for predicting bone growth over a 60-day treatment period. This computational challenge renders further design optimisation unfeasible for the development of customised bone scaffolds.

To address the abovementioned computational challenge, we develop a viable alternative, particularly suitable for design optimisation involving a large number of calculations with respect to different design variables. By leveraging the ML techniques, we significantly expedite the dynamic mechanobiological modelling process, making the time-dependent optimisation feasible within an acceptable timeframe. With the proposed ML-based framework, the computing time for predicting bone growth over a 60-day period can be reduced to just 6 min, involving only 16.66 h, 50 h, and 50 h for preparing the training datasets for the NN-3 used in the optimisation. This novel approach creates new possibilities for development of large-scale customised bone scaffolds, allowing for faster and more efficient exploration of design spaces and accelerating advancements in tissue engineering and regenerative medicine.

The ML approach adopted in this study has several advantages. First, all the neural networks exhibited good performances with sufficient accuracy. Second, NN-1 and NN-2 can directly output the nine and three independent elasticity and diffisivity parameters, respectively, whereas conventional methods such as regression or interpolation would require establishing twelve models for predicting the elasticity and diffusivity tensors. Third, the proposed ML models can be easily extended to consideration for all the 19 diameters of all rods in the isotruss lattice structure, as illustrated in Section 2.4.2. In addition, NN-3 can deal with up to 20 design variables for the vertical and lateral design cases.

In this study, we compared the stiffness of the established FE model with the in-house mechanical test, demonstrating that the FE model can provide a reliable basis for further optimisation studies. Concerning the numerical results, the optimised scaffold (uniform design, vertical and lateral gradient designs) outperformed the empirical design, yielding superior bone regeneration outcomes. This indicates that the gradient designs offer a larger design space and can further enhance the bone growth over time, which aligns with the previous findings [16,17,24] that mechanobiological optimisation has proven to be more meaningful for design of scaffolds. Notably, the lateral gradient design emerges as the most suitable for the sheep mandible case considered in this study, as it significantly enhances the formation of newly developed bony tissue in comparison with the other designs. This result can be attributed to the more effective mechanical stimuli and mass concentration provided by the lateral gradient design, which triggered better bone formation at an early stage. Such a similar result has also been reported by Pobloth et al. [66] and Perier-Metz et al. [67] . Note that these findings underscore the potential of the lateral gradient design in promoting bone regeneration in a specific context of the sheep mandible reconstruction.

Despite the efficiency and effectiveness of our proposed optimisation framework, there are a few limitations that remain for further investigation in the future studies. First, the choice of a fictitious time step of 3 days presents a trade-off; meaning that a smaller time step could enhance the accuracy of bone growth prediction but can significantly increase computational cost in the optimisation processes. Conversely, a larger time step might reduce computational cost but potentially compromise the accuracy of bone growth simulation. Further studies are needed in this regard to quantify the effect of a fictitious time step for determining a most suitable time interval.

Second, the bone growth-related parameters were obtained from the empirical constants or previous studies as summarised in Table 3. Although such data and predictive models established are of certain clinical implication, the optimised scaffolds are still

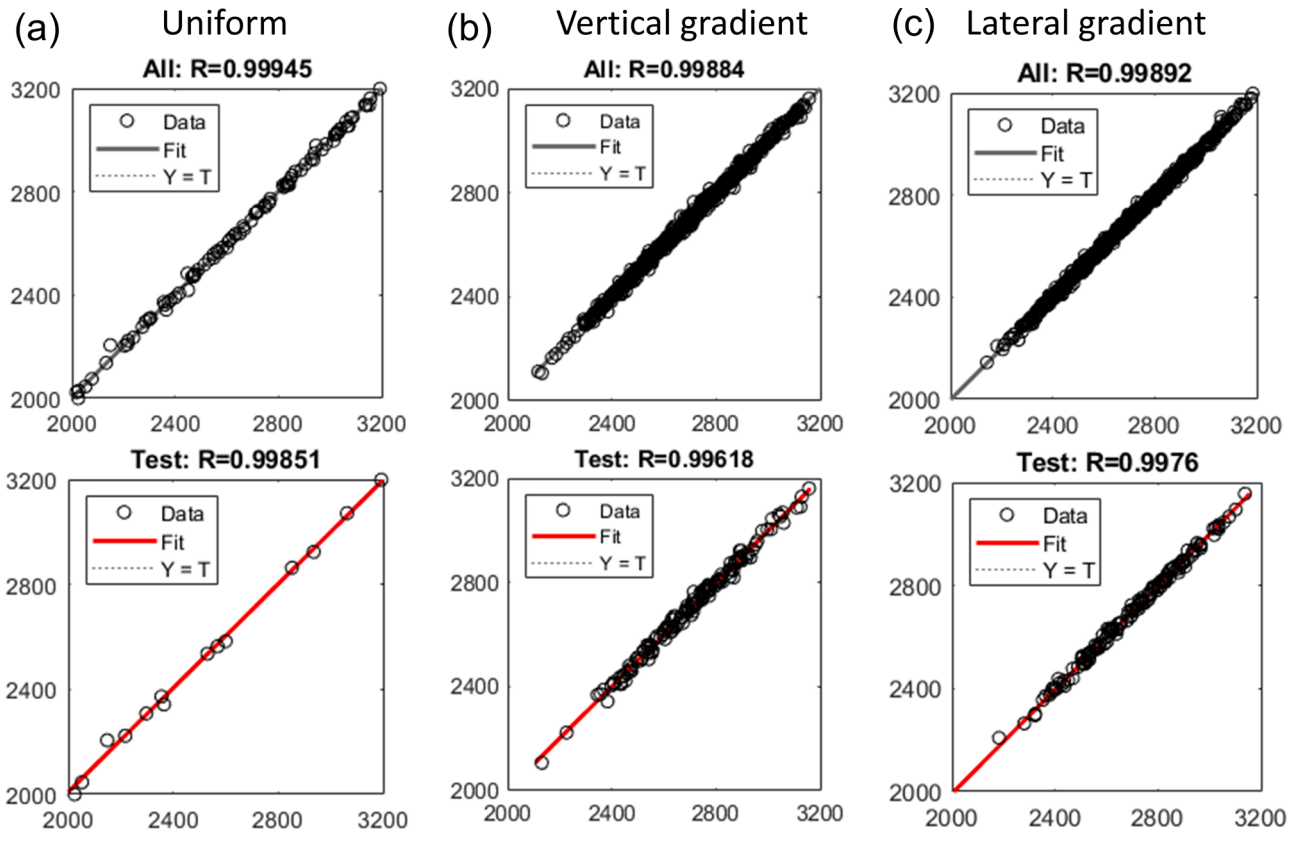

Fig. 9. Regression values of NN-3 for design optimisation performed on all the ground-truth data and test data. (a) Uniform design. (b) Vertical gradient design. (c) Lateral gradient design.

Table 6
The optimisation results of the empirical design and the four design schemes.

Design schemes		Optimised strut diameters (mm)	Total bone density (NN-3) g/cm^3	Total bone density (FEA) g/cm^3	Relative error
Empirical design		0.45, 0.45, 0.45, 045	–	2980.75	–
Uniform design		0.3, 0.53, 0.3, 0.45	3086.64	3038.41	1.59 %
Vertical gradient design	Area 1	0.303, 0.302, 0.306, 0.366	3305.17	3208.04	3.02 %
	Area 2	0.306, 0.655, 0.307, 0.329			
	Area 3	0.526, 0.305, 0.376, 0.664			
	Area 4	0.305, 0.595, 0.335, 0.394			
	Area 5	0.304, 0.306, 0.620, 0.300			
Lateral gradient design	Area 1	0.300, 0.301, 0.303, 0.442	3487.70	3529.50	−1.18&
	Area 2	0.307, 0.303, 0.300, 0.303			
	Area 3	0.345, 0.749, 0.425, 0.301			
	Area 4	0.301, 0.393, 0.301, 0.308			
	Area 5	0.301, 0.300, 0.302, 0.418			

required to be validated through specific *in vivo* studies, thereby demonstrating their effectiveness in comparison with the conventional empirical design.

Third, while we utilised the isotruss lattice as a base structure for the design of scaffold unit cell to showcase the effectiveness of the optimisation framework, it is important to emphasise that the proposed approach is not limited to this particular lattice type. While the isotruss lattice ensures the absence of free ends between adjacent gradient regions, variations in strut size may lead to strain/stress concentration at connecting points. To address this issue, post-processing involving gradual changes in strut size could offer a simple solution when fabricating the optimised gradient scaffolds.

Fourth, division of gradient areas within the scaffold was based on empirical experience, which may not encompass all possible configurations for achieving the most favourable bone ingrowth outcomes. Exploring alternative gradient patterns and investigating their impact on bone growth is imperative to identify optimal designs. Ideally, each RVE in the scaffold should possess its own set of design variables, enabling customisation to maximise bone ingrowth capability. However, this approach would exponentially increase the number of design variables, possibly rendering non-gradient optimisation methods inefficient.

5. Conclusion

This study introduces a novel dynamic optimisation framework for the gradient design of patient-specific scaffolds by leveraging machine learning (ML) techniques. The optimisation results unveiled that the lateral gradient design outperformed the uniform and vertical gradient designs, demonstrating that an optimal bone growth outcome can be achieved through a rational customisation of scaffold with graded microstructures. By harnessing the power of ML techniques, this study holds the promise of shedding new light on mechanobiological design for tailoring bulk scaffolds for treating critical size defects. The integration of machine learning into the optimisation procedure offers promising opportunities to enhance the efficiency and efficacy of scaffold design, ultimately leading to advancements in tissue engineering and regenerative medicine.

CRediT authorship contribution statement

Chi Wu: Conceptualization, Data curation, Formal analysis, Investigation, Methodology, Software, Validation, Visualization, Writing – original draft, Writing – review & editing. **Boyang Wan:** Data curation, Formal analysis, Writing – original draft. **Yanan Xu:** Investigation, Methodology. **D S Abdullah Al Maruf:** Investigation, Project administration. **Kai Cheng:** Methodology, Writing – original draft. **William T Lewin:** Writing – original draft. **Jianguang Fang:** Resources, Supervision, Writing – review & editing. **Hai Xin:** Writing – original draft. **Jeremy M Crook:** Project administration, Resources. **Jonathan R Clark:** Conceptualization, Funding acquisition, Project administration, Resources, Supervision. **Grant P Steven:** Supervision, Writing – review & editing, Funding acquisition. **Qing Li:** Conceptualization, Funding acquisition, Project administration, Resources, Supervision, Writing – review & editing.

Declaration of competing interest

The authors declare that they have no known competing financial interests or personal relationships that could have appeared to influence the work reported in this paper.

Data availability

The related code, trained neural networks, will be made available on request.

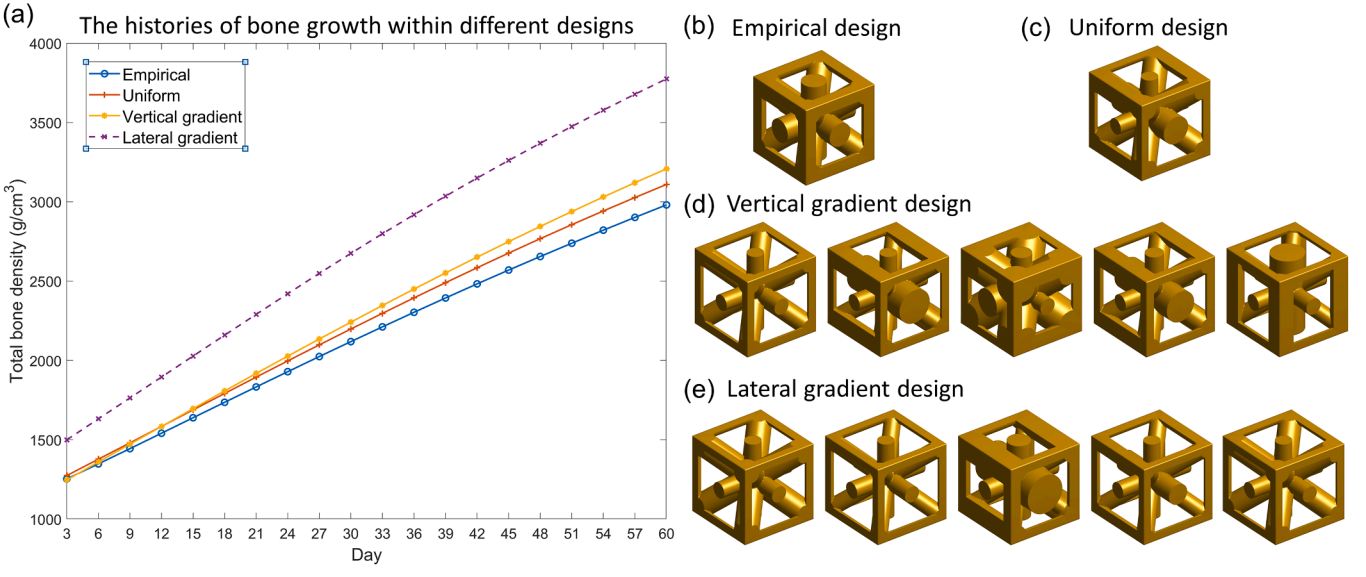

Fig. 10. Comparison of the results for the empirical design, uniform design, vertical gradient design and lateral gradient design. (a) The histories of bone growth over 60 days. (b)-(e) The iso-truss structures.

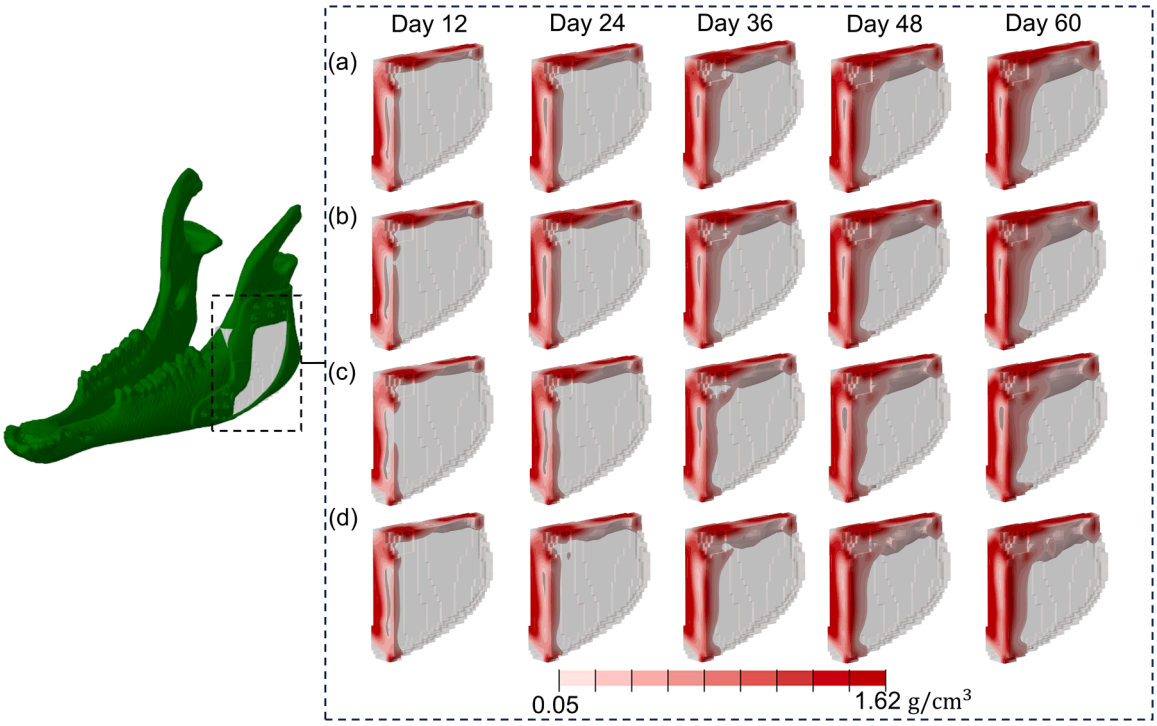

Fig. 11. Comparison of the newly formed bone distribution on Days 12, 24, 36, 48 and 60. (a) Empirical design. (b) Uniform design. (c) Vertical gradient design. (d) Lateral gradient design.

Acknowledgements

The support from the Australian Research Council (ARC) through the Discovery project (DP230103180) is acknowledged. The supports from the National Health and Medical Research Council (NHMRC) Centre of Research Excellence (2024602) as well as the Cancer Institute New South Wales (CINSW 2020/2081), Sydney Local Health District and the Lang Walker Family Foundation are acknowledged. The Arto Hardy Family for their generous support of the Biomedical Innovation Hub at Chris O'Brien Lifehouse and the Australian Government through the Sarcoma and Surgical Research Centre is acknowledged.

References

[1] L. Vidal, C. Kampleitner, M.A. Brennan, A. Hoornaert, P. Layrolle, Reconstruction of Large Skeletal Defects: current Clinical Therapeutic Strategies and Future Directions Using 3D Printing, Front. Bioeng. Biotechnol. 8 (2020) 61.
[2] C. Wu, A. Entezari, K. Zheng, J. Fang, H. Zreiqat, G.P. Steven, M.V. Swain, Q. Li, A machine learning-based multiscale model to predict bone formation in scaffolds, Nat. Comput. Sci. 1 (8) (2021) 532–541.
[3] C. Wu, J.G. Fang, A. Entezari, G.Y. Sun, M.V. Swain, Y.N. Xu, G.P. Steven, Q. Li, A time-dependent mechanobiology-based topology optimization to enhance bone growth in tissue scaffolds, J. Biomech. (2021).
[4] A. Entezari, N.C. Liu, Z. Zhang, J. Fang, C. Wu, B. Wan, M. Swain, Q. Li, Nondeterministic multiobjective optimization of 3D printed ceramic tissue scaffolds, J. Mech. Behav. Biomed. Mater. 138 (2023) 105580.
[5] Y.Z. Wu, J.G. Fang, C. Wu, C.Y. Li, G.Y. Sun, Q. Li, Additively manufactured materials and structures: a state-of-the-art review on their mechanical characteristics and energy absorption, Int. J. Mech. Sci. 246 (2023) 108102.
[6] P.S. Poh, T. Lingner, S. Kalkhof, S. Mardian, J. Baumbach, P. Dondl, G.N. Duda, S. Checa, Enabling technologies towards personalization of scaffolds for large bone defect regeneration, Curr. Opin. Biotechnol. 74 (2022) 263–270.
[7] C. Metz, G.N. Duda, S. Checa, Towards multi-dynamic mechano-biological optimization of 3D-printed scaffolds to foster bone regeneration, Acta Biomater. 101 (2020) 117–127.
[8] C. Jiao, D.Q. Xie, Z.J. He, H.X. Liang, L.D. Shen, Y.W. Yang, Z.J. Tian, G.F. Wu, C.J. Wang, Additive Manufacturing of Bio-inspired ceramic bone Scaffolds: structural Design, mechanical properties and biocompatibility, Mater. Des. 217 (2022) 110610.
[9] J.E. Cadman, S. Zhou, Y. Chen, Q. Li, On design of multi-functional microstructural materials, J. Mater. Sci. 48 (2013) 51–66.
[10] N. Uth, J. Mueller, B. Smucker, A.M. Yousefi, Validation of scaffold design optimization in bone tissue engineering: finite element modeling versus designed experiments, Biofabrication 9 (1) (2017) 015023.
[11] P.S.P. Poh, D. Valainis, K. Bhattacharya, M. van Griensven, P. Dondl, Optimization of bone scaffold porosity distributions, Sci. Rep. 9 (1) (2019) 9170.
[12] N. Abbasi, S. Hamlet, R.M. Love, N.T. Nguyen, Porous scaffolds for bone regeneration, J. Sci. Adv. Mater. Devices 5 (1) (2020) 1–9.
[13] A. Boccaccio, A.E. Uva, M. Fiorentino, L. Lamberti, G. Monno, A mechanobiology-based algorithm to optimize the microstructure geometry of bone tissue scaffolds, Int J Biol Sci 12 (1) (2016) 1–17.
[14] G. Percoco, A.E. Uva, M. Fiorentino, M. Gattullo, V.M. Manghisi, A. Boccaccio, Mechanobiological approach to design and optimize bone tissue scaffolds 3D printed with fused deposition modeling: a feasibility study, Materials 13 (3) (2020) 648.
[15] C. Wu, J. Fang, A. Entezari, G. Sun, M.V. Swain, Y. Xu, G.P. Steven, Q. Li, A time-dependent mechanobiology-based topology optimization to enhance bone growth in tissue scaffolds, J. Biomech. 117 (2021) 110233.

[16] D.O. Cohen, S.M.G. Aboutaleb, A.W. Johnson, J.A. Norato, Bone adaptation-driven design of periodic scaffolds, J. Mech. Des. 143 (12) (2021).
[17] C. Perier-Metz, G.N. Duda, S. Checa, A mechanobiological computer optimization framework to design scaffolds to enhance bone regeneration, Front. Bioeng. Biotechnol. 10 (2022) 980727.
[18] J.A. Sanz-Herrera, J.M. Garcia-Aznar, M. Doblare, On scaffold designing for bone regeneration: a computational multiscale approach, Acta Biomater. 5 (1) (2009) 219–229.
[19] S.I. Roohani-Esfahani, C.R. Dunstan, J.J. Li, Z. Lu, B. Davies, S. Pearce, J. Field, R. Williams, H. Zreiqat, Unique microstructural design of ceramic scaffolds for bone regeneration under load, Acta Biomater. 9 (6) (2013) 7014–7024.
[20] S. Wu, X. Liu, K.W. Yeung, C. Liu, X. Yang, Biomimetic porous scaffolds for bone tissue engineering, Mater. Sci. Eng. R 80 (2014) 1–36.
[21] M.O. Al-Barqawi, B. Church, M. Thevamaran, D.J. Thoma, A. Rahman, Design and validation of additively manufactured metallic cellular scaffold structures for bone tissue engineering, Materials 15 (9) (2022) 3310.
[22] D. Luo, Q. Rong, Q. Chen, Finite-element design and optimization of a three-dimensional tetrahedral porous titanium scaffold for the reconstruction of mandibular defects, Med. Eng. Phys. 47 (2017) 176–183.
[23] Y. Chen, S. Zhou, Q. Li, Microstructure design of biodegradable scaffold and its effect on tissue regeneration, Biomaterials 32 (22) (2011) 5003–5014.
[24] C. Perier-Metz, G.N. Duda, S. Checa, Initial mechanical conditions within an optimized bone scaffold do not ensure bone regeneration–an in silico analysis, Biomech. Model. Mechanobiol. 20 (5) (2021) 1723–1731.
[25] S. Sturm, S. Zhou, Y.W. Mai, Q. Li, On stiffness of scaffolds for bone tissue engineering-a numerical study, J. Biomech. 43 (9) (2010) 1738–1744.
[26] C. Perier-Metz, A. Cipitria, D.W. Hutmacher, G.N. Duda, S. Checa, An in silico model predicts the impact of scaffold design in large bone defect regeneration, Acta Biomater. 145 (2022) 329–341.
[27] C. Wu, K.K. Zheng, J.G. Fang, G.P. Steven, Q. Li, Time-dependent topology optimization of bone plates considering bone remodeling, Comput. Methods Appl. Mech. Eng. 359 (2020).
[28] M. Shirzad, A. Zolfagharian, A. Matbouei, M. Bodaghi, Design, evaluation, and optimization of 3D printed truss scaffolds for bone tissue engineering, J. Mech. Behav. Biomed. Mater. 120 (2021) 104594.
[29] J. Roberge, J. Norato, Computational design of curvilinear bone scaffolds fabricated via direct ink writing, Comput. Aided Des. 95 (2018) 1–13.
[30] M.R. Dias, J.M. Guedes, C.L. Flanagan, S.J. Hollister, P.R. Fernandes, Optimization of scaffold design for bone tissue engineering: a computational and experimental study, Med. Eng. Phys. 36 (4) (2014) 448–457.
[31] A.H. Foroughi, M.J. Razavi, Multi-objective shape optimization of bone scaffolds: enhancement of mechanical properties and permeability, Acta Biomater. 146 (2022) 317–340.
[32] W. Chen, N. Dai, J. Wang, H. Liu, D. Li, L. Liu, Personalized design of functional gradient bone tissue engineering scaffold, J. Biomech. Eng. 141 (11) (2019).
[33] S. Kanwar, S. Vijayavenkataraman, 3D printable bone-mimicking functionally gradient stochastic scaffolds for tissue engineering and bone implant applications, Mater. Des. 223 (2022) 111199.
[34] A.H. Foroughi, M.J. Razavi, Shape optimization of orthopedic porous scaffolds to enhance mechanical performance, J. Mech. Behav. Biomed. Mater. 128 (2022) 105098.
[35] M.K. Heljak, W. Swieszkowski, C.X. Lam, D.W. Hutmacher, K.J. Kurzydlowski, Evolutionary design of bone scaffolds with reference to material selection, Int. J. Numer. Method Biomed. Eng. 28 (6–7) (2012) 789–800.
[36] S. Vijayavenkataraman, L. Zhang, S. Zhang, J.Y. Hsi Fuh, W.F. Lu, Triply periodic minimal surfaces sheet scaffolds for tissue engineering applications: an optimization approach toward biomimetic scaffold design, ACS Appl. Bio. Mater. 1 (2) (2018) 259–269.
[37] S. Xu, S. Zhang, G. Ren, Y. Pan, J. Li, Optimization of structural and processing parameters for selective laser melting of porous 316L bone scaffolds, Materials 15 (17) (2022) 5896.
[38] H. Kang, C.Y. Lin, S.J. Hollister, Topology optimization of three dimensional tissue engineering scaffold architectures for prescribed bulk modulus and diffusivity, Struct. Multidiscipl. Optim. 42 (4) (2010) 633–644.
[39] J. Wieding, A. Wolf, R. Bader, Numerical optimization of open-porous bone scaffold structures to match the elastic properties of human cortical bone, J. Mech. Behav. Biomed. Mater. 37 (2014) 56–68.
[40] S. Rashia Begum, M. Saravana Kumar, C. Pruncu, M. Vasumathi, P. Harikrishnan, Optimization and fabrication of customized scaffold using Addit. Manuf. to match the property of human bone, J. Mater. Eng. Perform. (2021) 1–12.
[41] W. Wojnicz, M. Augustyniak, P. Borzyszkowski, Mathematical approach to design 3D scaffolds for the 3D printable bone implant, Biocybernetics Biomed. Eng. 41 (2) (2021) 667–678.
[42] L. Colabella, A. Cisilino, V. Fachinotti, C. Capiel, P. Kowalczyk, Multiscale design of artificial bones with biomimetic elastic microstructures, J. Mech. Behav. Biomed. Mater. 108 (2020) 103748.
[43] C.Y. Lin, N. Kikuchi, S.J. Hollister, A novel method for biomaterial scaffold internal architecture design to match bone elastic properties with desired porosity, J. Biomech. 37 (5) (2004) 623–636.
[44] T.H.V. Pires, J.W.C. Dunlop, A.P.G. Castro, P.R. Fernandes, Wall shear stress analysis and optimization in tissue engineering TPMS scaffolds, Materials 15 (20) (2022) 7375.
[45] Y. Chen, M. Schellekens, S. Zhou, J. Cadman, W. Li, R. Appleyard, Q. Li, Design optimization of scaffold microstructures using wall shear stress criterion towards regulated flow-induced erosion, J. Biomech. Eng. 133 (8) (2011) 081008.
[46] A. Boccaccio, M. Fiorentino, A.E. Uva, L.N. Laghetti, G. Monno, Rhombicuboctahedron unit cell based scaffolds for bone regeneration: geometry optimization with a mechanobiology - driven algorithm, Mater. Sci. Eng. C Mater. Biol. Appl. 83 (2018) 51–66.
[47] O.L. Rodriguez-Montano, C.J. Cortes-Rodriguez, F. Naddeo, A.E. Uva, M. Fiorentino, A. Naddeo, N. Cappetti, M. Gattullo, G. Monno, A. Boccaccio, Irregular load adapted scaffold optimization: a computational framework based on mechanobiological criteria, ACS Biomater. Sci. Eng 5 (10) (2019) 5392–5411.
[48] A. Boccaccio, A.E. Uva, M. Fiorentino, G. Mori, G. Monno, Geometry design optimization of functionally graded scaffolds for bone tissue engineering: a mechanobiological approach, PLoS One 11 (1) (2016) e0146935.
[49] E.F. Lehder, I.A. Ashcroft, R.D. Wildman, L.A. Ruiz-Cantu, I. Maskery, A multiscale optimisation method for bone growth scaffolds based on triply periodic minimal surfaces, Biomech. Model. Mechanobiol. 20 (6) (2021) 2085–2096.
[50] K. Zheng, N. Yoda, J. Chen, Z. Liao, J. Zhong, C. Wu, B. Wan, S. Koyama, K. Sasaki, C. Peck, M. Swain, Q. Li, Bone remodeling following mandibular reconstruction using fibula free flap, J. Biomech. 133 (2022) 110968.
[51] V. Orassi, G.N. Duda, M. Heiland, H. Fischer, C. Rendenbach, S. Checa, Biomechanical assessment of the validity of sheep as a preclinical model for testing mandibular fracture fixation devices, Front. Bioeng. Biotechnol. 9 (2021) 672176.
[52] M. Timoumi, N. Barhoumi, A. Znaidi, A. Maazouz, K. Lamnawar, Mechanical behavior of 3D-printed PEEK and its application for personalized orbital implants with various infill patterns and densities, J. Mech. Behav. Biomed. Mater. 136 (2022) 105534.
[53] R.M. Grzeskowiak, J. Schumacher, M.S. Dhar, D.P. Harper, P.Y. Mulon, D.E. Anderson, Bone and cartilage interfaces with orthopedic implants: a literature review, Front. Surg. 7 (2020) 601244.
[54] B.M. Ferguson, A. Entezari, J. Fang, Q. Li, Optimal placement of fixation system for scaffold-based mandibular reconstruction, J. Mech. Behav. Biomed. Mater. 126 (2022) 104855.
[55] J.A. Sanz-Herrera, J.M. Garcia-Aznar, M. Doblare, A mathematical model for bone tissue regeneration inside a specific type of scaffold, Biomech. Model. Mechanobiol. 7 (5) (2008) 355–366.
[56] J.F. Bourgat, Numerical Experiments of the Homogenization method, Lecture Notes in Mathematics, Springer Berlin Heidelberg, 1979, pp. 330–356.
[57] C. Wu, A. Entezari, K.K. Zheng, J.G. Fang, H. Zreiqat, G.P. Steven, M.V. Swain, Q. Li, A machine learning-based multiscale model to predict bone formation in scaffolds, Nat. Comput. Sci. 1 (8) (2021) 532–541.
[58] G.S. Beaupre, T.E. Orr, D.R. Carter, An approach for time-dependent bone modeling and remodeling–theoretical development, J. Orthop. Res. 8 (5) (1990) 651–661.

[59] S. Ogawa, T. Yamada, Topology optimization for transient thermomechanical coupling problems, Appl. Math. Model. 109 (2022) 536–554.
[60] S. Watts, D.A. Tortorelli, A geometric projection method for designing three-dimensional open lattices with inverse homogenization, Int. J. Numer. Methods Eng. 112 (11) (2017) 1564–1588.
[61] R. Tonello, K. Conradsen, D.B. Pedersen, J.R. Frisvad, Surface roughness and grain size variation when 3d printing polyamide 11 parts using selective laser sintering, Polymers 15 (13) (2023) 2967.
[62] A. Florian, An efficient sampling scheme: updated latin hypercube sampling, Probab. Eng. Mech. 7 (2) (1992) 123–130.
[63] C. Wu, J. Luo, J. Zhong, Y. Xu, B. Wan, W. Huang, J. Fang, G.P. Steven, G. Sun, Q. Li, Topology optimisation for design and Addit. Manuf. of functionally graded lattice structures using derivative-aware machine learning algorithms, Addit. Manuf. 78 (2023) 103833.
[64] C.R. Houck, J. Joines, M.G. Kay, A genetic algorithm for function optimization: a Matlab implementation, Ncsu-ie tr 95 (09) (1995) 1–10.
[65] C. Wu, B. Wan, A. Entezari, J. Fang, Y. Xu, Q. Li, Machine learning-based design for Addit. Manuf. in biomedical engineering, Int. J. Mech. Sci. 266 (2024) 108828.
[66] A.M. Pobloth, S. Checa, H. Razi, A. Petersen, J.C. Weaver, K. Schmidt-Bleek, M. Windolf, A.Á. Tatai, C.P. Roth, K.D. Schaser, G.N. Duda, P. Schwabe, Mechanobiologically optimized 3D titanium-mesh scaffolds enhance bone regeneration in critical segmental defects in sheep, Sci. Transl. Med. 10 (423) (2018).
[67] C. Perier-Metz, A. Cipitria, D.W. Hutmacher, G.N. Duda, S. Checa, An in silico model predicts the impact of scaffold design in large bone defect regeneration, Acta Biomater. (2022).